Why coronal mass ejections arrive differently: solar cycle modulation through solar wind structure

Gyeltshen, D. L. ORCID: https://orcid.org/0009-0004-8411-7042, Barnard, L. A. ORCID: https://orcid.org/0000-0001-9876-4612, Owens, M. J. ORCID: https://orcid.org/0000-0003-2061-2453 and Riley, P. ORCID: https://orcid.org/0000-0002-1859-456X (2026) Why coronal mass ejections arrive differently: solar cycle modulation through solar wind structure. Space Weather, 24 (4). e2025SW004667. ISSN 1542-7390 doi: 10.1029/2025SW004667 Available at https://centaur.reading.ac.uk/129181/

Space Weather

RESEARCH ARTICLE
10.1029/2025SW004667

Why Coronal Mass Ejections Arrive Differently: Solar Cycle Modulation Through Solar Wind Structure

D. L. Gyeltshen[1,2], **L. A. Barnard**[1], **M. J. Owens**[1], **and P. Riley**[3]

[1]Department of Meteorology, University of Reading, Reading, UK, [2]National Centre for Hydrology and Meteorology, Royal Government of Bhutan, Thimphu, Bhutan, [3]Predictive Science Inc., San Diego, CA, USA

Key Points:

- Identical CMEs were simulated to propagate through 18,000 instances of realistically structured solar wind over 4.5 solar cycles
- CME transit time/arrival speed at 1 AU can vary up to 47 hr/340 km s^{-1} due to the changing ambient solar wind structure
- CME transit time and arrival speed show greater short-term variability during solar minimum/declining phase than solar maximum/rising phase

Correspondence to:

D. L. Gyeltshen,
d.l.gyeltshen@pgr.reading.ac.uk

Citation:

Gyeltshen, D. L., Barnard, L. A., Owens, M. J., & Riley, P. (2026). Why Coronal Mass Ejections arrive differently: Solar cycle modulation through Solar wind structure. *Space Weather*, *24*, e2025SW004667. https://doi.org/10.1029/2025SW004667

Received 8 AUG 2025
Accepted 17 MAR 2026

Author Contributions:

Conceptualization: D. L. Gyeltshen, L. A. Barnard, M. J. Owens, P. Riley
Data curation: P. Riley
Formal analysis: D. L. Gyeltshen
Investigation: D. L. Gyeltshen
Methodology: D. L. Gyeltshen, L. A. Barnard, M. J. Owens
Software: D. L. Gyeltshen, L. A. Barnard, M. J. Owens
Supervision: L. A. Barnard, M. J. Owens
Visualization: D. L. Gyeltshen, L. A. Barnard, M. J. Owens
Writing – original draft: D. L. Gyeltshen
Writing – review & editing: L. A. Barnard, M. J. Owens, P. Riley

Abstract

Coronal Mass Ejections (CMEs) are large structures of magnetized plasma ejected from the Sun's atmosphere into the heliosphere. The interaction of CMEs with the ambient solar wind during propagation affects arrival time and speed at Earth. Since the solar wind structure changes with the solar cycle, variability in the transit times and arrival speeds of CMEs should also change systematically with the solar cycle. We use a solar wind model, HUXt, to conduct simulations of the same CME propagating through realistic ambient solar wind environments from 1975 to 2024 inclusive. We conduct this experiment with an "average" CME, with an initial speed of 495 km s^{-1} and a full angular width of 37.4°, and a "fast" CME, with a speed of 1,070 km s^{-1} and an angular width of 69.8°. We find that lower solar activity is associated with increased variability in both transit time to Earth and arrival speed at Earth. For the average CME, the average short-term variability (i.e., inter-quartile range within a Carrington rotation) in transit time was 22.4 hr during solar minimum and 16.4 hr during solar maximum. The fast CME demonstrated reduced variability, with corresponding values of 18.2 and 12.5 hr. Similar trends in variability were found for arrival speeds. This suggests that for a given CME, arrival times and speeds at Earth are more predictable at solar maximum than solar minimum. Furthermore, comparing transition phases of the solar cycle, the declining phase was found to be more variable than the rising phase.

Plain Language Summary

Space-weather events can have wide-reaching socioeconomic impacts, including disruptions to electrical power grids, failures in Global Navigation Satellite Systems like GPS, and risks to human health. Consequently, the ability to reliably forecast the arrival of space-weather phenomena such as Coronal Mass Ejections (CMEs) is essential. CMEs are eruptions of magnetized plasma from the Sun's atmosphere into the heliosphere, where they interact with the solar wind. As the solar wind is known to vary throughout the solar cycle, this study explored whether the transit times and arrival speeds of CMEs depend on the phase of the solar cycle. To do this, numerical simulations were used to model CMEs arrival characteristics at Earth. The spread of the results indicated greater variability in both transit time and arrival speed during solar minimum. This implies that predicting CME arrival time and speed may be challenging during periods of solar minimum.

1. Introduction

Space weather encompasses the temporal variations in space that impact human lives, with emphasis on the near-Earth environment. The resultant electromagnetic radiation, solar energetic particles and geomagnetic storms affect the Earth's magnetosphere, thermosphere, ionosphere, and ground-based infrastructure. Space-weather events have major socioeconomic impacts because of our increasing use of space and our dependence on space-based technologies. Extreme space weather events cause disruptions to satellite operation, navigation systems, radio communication, power grids, and rail networks, and also expose humans in space or on high-altitude flights to harmful radiation doses and energetic particles (Cannon, 2013; Eastwood et al., 2017). Although mitigation procedures are being developed and refined, their efficacy relies on the accuracy of space weather forecasts. For example, Oughton et al. (2019) found that for the UK alone, electricity infrastructure failures caused by an extreme space weather event could result in losses of £16 billion without forecasting, £3 billion with the current forecast skill level and £0.9 billion with enhanced forecasting. As such, understanding causal phenomena such as solar eruptive processes and high-speed solar wind remains a high priority for improving prediction accuracies (Buzulukova & Tsurutani, 2022). Here, we focus on Coronal Mass Ejections (CMEs), which are the drivers of the most severe space weather (Gosling, 1993; Richardson et al., 2002).

CMEs are large structures comprising plasma and accompanying magnetic field ejected from the Sun's atmosphere into the heliosphere. The coherent magnetic field structure of a CME, the highly variable sheath region ahead of the CME, and the initial shock front can all contribute to driving geomagnetic storms and solar energetic particle events (Gopalswamy, 2016). In this context, it is in the interest of forecast centers to correctly predict CME arrival time and properties at Earth. CMEs have a typical Sun-Earth transit time, τ, of 1–5 days and are forecast using a combination of observations and modeling. Initially, CMEs at the Sun are typically detected and characterized using remotely sensed data of solar disturbances from coronagraphs onboard spacecraft like SOHO (Solar and Heliospheric Observatory, Brueckner et al., 1995) and STEREO (Solar Terrestrial Relations Observatory, Howard et al., 2008). Then, the parameters are fed into propagation models—these may be empirical models, expansion speed models, drag-based models, physics-based models, Magnetohydrodynamic (MHD) models, etc.—to calculate arrival time and other variables (Temmer et al., 2023; Zhao & Dryer, 2014).

Riley et al. (2018) found that the mean absolute error in τ forecasts from 32 distinct models was 14.0 hr, with a standard deviation of 18.3 hr. A subsequent study by Kay et al. (2024) showed that the current situation remains similar, with the updated mean absolute error in τ being 13.2 hr with a standard deviation of 17.4 hr. While the models used to make such forecasts are imperfect, these errors largely stem from two main sources of observational uncertainty: in CME parameters and in ambient solar wind conditions. The extents of their contributions vary, and isolating individual error contributions for observed events is difficult. Riley and Ben-Nun (2021) suggested an uncertainty in τ of ±7 hr arising from uncertainty in the ambient solar wind alone. However, this was for a very specific case, being derived by propagating a CME through an ensemble of 12 ambient solar wind solutions for Carrington Rotation (CR) number 2,207 (2–29 September 2018). The ensemble was built using magnetogram realizations from the ADAPT (Air Force Data Assimilative Photospheric flux Transport) model (Arge et al., 2010).

The ambient solar wind results from the extension of the solar atmosphere into space; it forms a persistent outflow of plasma and magnetic field into interplanetary space (e.g., M. J. Owens, 2020, and references therein). CMEs interact with the ambient solar wind during propagation, leading to dynamic modulation of their properties, particularly velocity. In general, slow CMEs tend to accelerate, whereas fast CMEs experience deceleration due to drag forces exerted by the background solar wind (Cargill, 2004; Gopalswamy et al., 2000; Vršnak & Žic, 2007). Numerous studies have shown a significant effect of ambient solar wind speed on CME τ (Case et al., 2008; Shanmugaraju & Vršnak, 2014; Vršnak & Žic, 2007). However, the structure and properties of the ambient solar wind are not static. In particular, the ambient solar wind properties exhibit substantial variability over the solar cycle (i.e., 11-year Schwabe cycle of solar magnetic activity) (Manoharan, 2012). Observations from the Ulysses spacecraft revealed a highly bimodal ambient solar wind structure during solar minimum, with "slow" streamer-belt wind dominating at lower heliolatitudes and "fast" coronal-hole wind at higher heliolatitudes (Ebert et al., 2009; McComas et al., 2000, 2003). On the other hand, the solar wind during solar maximum has less latitudinal variation with slow and fast wind interleaved throughout. This variation in solar wind structure is likely to have solar cycle phase-dependent implications for CME τ and hence for CME arrival time forecasts.

A possible solar cycle trend in τ variability was recently suggested by Kay et al. (2024). They analyzed τ-prediction errors by compiling a data set of genuine CME forecasts submitted by a range of community models between 2013 and 2023. The largest τ errors were observed at solar minimum, though also the largest τ values, presumably due to the prevalence of slower CMEs. Normalizing errors by τ significantly reduced the solar-cycle trend, but some residual patterns remained, implying other underlying sources of variability. However, the higher degrees of freedom associated with observed events make it difficult to determine the exact causal factor(s), that is, do the errors primarily result from uncertainty in the CME parameters or uncertainty in the ambient solar wind? Are there solar-cycle trends in CME parameters, as well as ambient solar wind? Here, we attempt to isolate the effect of the changing solar wind structure on CME τ error. We do this by limiting all other potential factors, such as CME frequency, CME properties, and CME-CME interactions. We only allow ambient solar wind conditions to vary (section (2.1)) by using a reduced-physics solar wind model (section (2.2)) to simulate realistic solar wind conditions over multiple solar cycles.

Although analysis in this study primarily focuses on CME transit time to Earth, we investigate another equally important parameter: CME speed at Earth, V_{1AU}. While τ is crucial for taking decisive mitigation steps against geomagnetic storms, V_{1AU} provides further information on a CME's geo-effectiveness, which could reduce losses caused by false alarms (M. J. Owens, Lockwood, and Barnard, 2020).

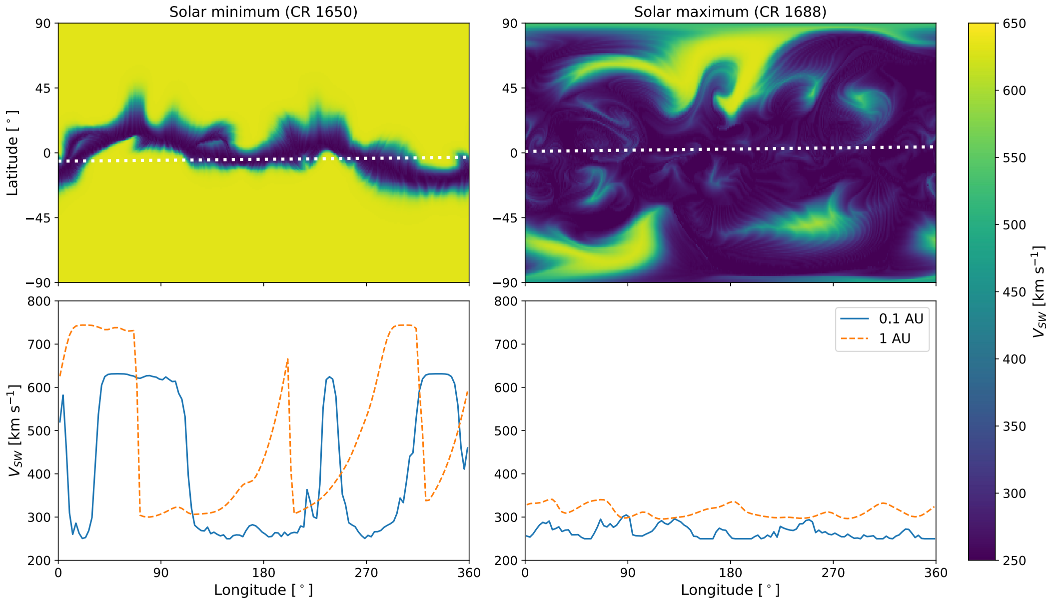

Figure 1. Top: 2-D plot of backmapped MAS solutions for radial solar wind speed, V_{SW} in km s^{-1} at 21.5 $R_\odot$ for solar minimum (CR 1650) (left) and solar maximum (CR 1688) (right). Dotted line shows Earth latitude. Bottom: solar wind speed as a function of Carrington longitude at Earth latitude for the same; blue for 21.5 $R_\odot$ and orange for 215 $R_\odot$.

To ensure the generality of our conclusions, we perform simulations for a statistically average CME and a typical fast CME. For each, we determine how the range of τ and V_{1AU} within a Carrington rotation (CR) varies over the solar cycle. This provides a measure of the predictability of these properties over the solar cycle in the absence of accurate ambient solar wind forecasting (e.g., M. J. Owens et al., 2008). It allows us to evaluate the change in baseline predictability of CME properties, independent of real-time solar wind uncertainties.

We describe the data sets for the ambient solar wind, solar cycle classification, and the average and fast CME parameters in Section 2.1. A brief explanation of the HUXt model and its setup for this experiment is presented in Section 2.2 and Section 2.3, respectively. Section 3 compares the resultant CME τ and V_{1AU} for different solar cycle phases, focusing on their variability within a Carrington rotation. A discussion of our results is provided in Section 4 and concluded in Section 5.

2. Methodology

2.1. Data

Solar wind models typically have an inner boundary at approximately 0.1 AU (21.5 $R_\odot$). The ambient solar wind conditions at the inner boundary are specified by the output of coronal model solutions based on the observed photospheric magnetic field. For example, the UK Met Office Space-weather Operations Center (Bingham et al., 2018) uses the semi-empirical Wang-Sheely-Arge (WSA) coronal model (Arge et al., 2003) to specify the radial solar wind speed and magnetic field at 0.1 AU, which serves as input to the Enlil MHD solar wind model (Odstrcil, 2003). Although WSA is used operationally, here we use the Magnetohydrodynamic Algorithm outside a Sphere (MAS) coronal model (Linker et al., 1999; Riley et al., 2012) (obtained from https://www.predsci.com/mhdweb/home.php), due to the pre-existing archive of solutions back to 1975.

The solar wind speeds used here correspond to the MAS output at 30 $R_\odot$, processed for use in the heliospheric MAS (helioMAS) model, that is, the speed is estimated using empirical relations to the MAS coronal magnetic field structure, in a similar manner to the WSA model. Also note that in this context, "solar wind speed" refers specifically to the radial component. In order to emulate operational forecasting results, we "backmap" the MAS solution from 30 to 21.5 $R_\odot$, accounting for continued solar wind acceleration (Section 2.2). In practice, this is a small change (a few % in speed and a degree or two shift in longitude). Figure 1 illustrates examples of this backmapped solution for solar minimum (CR 1650) and solar maximum (CR 1688), along with the Earth's

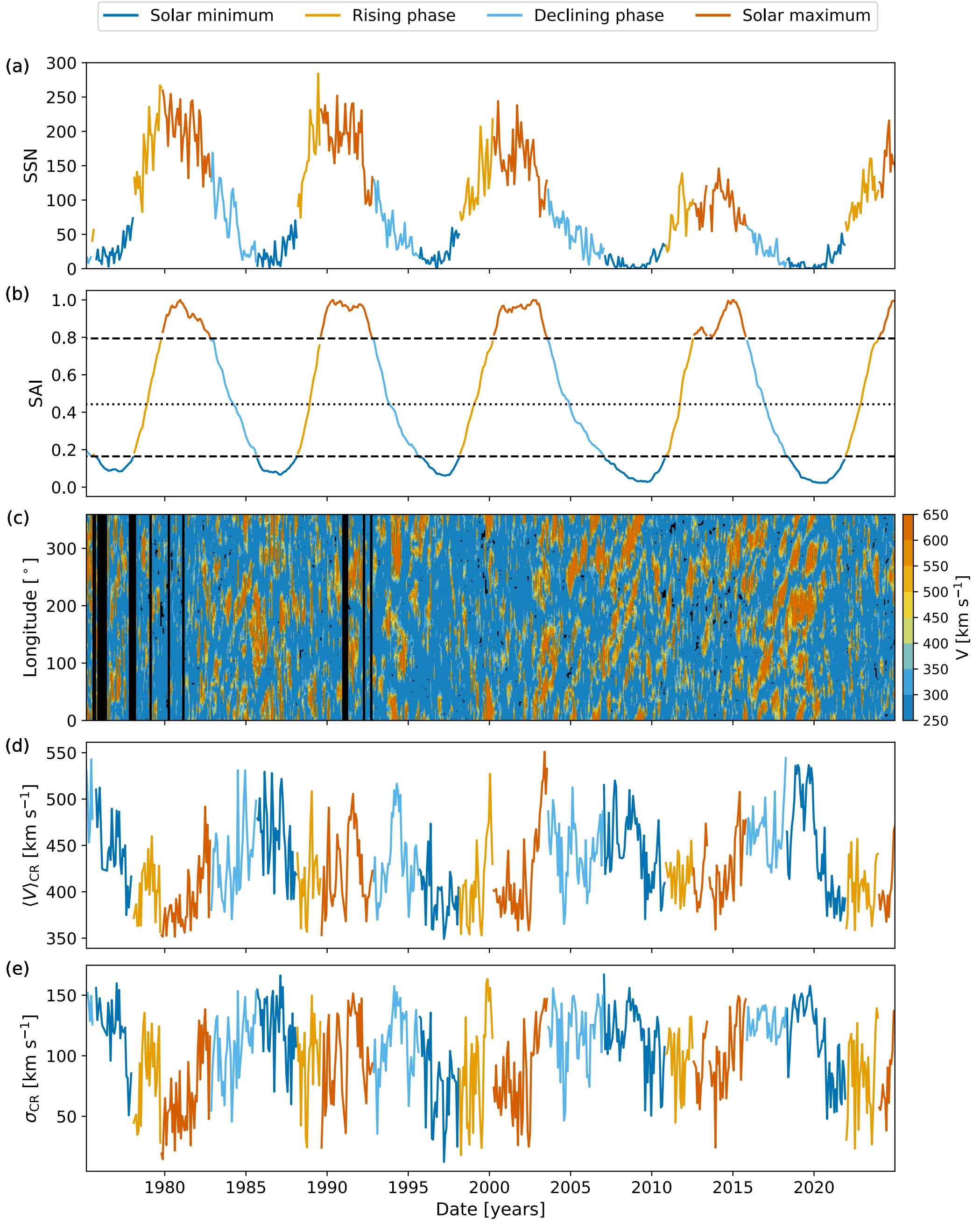

Figure 2. (a) Time series of monthly solar sunspot number (SSN). Intervals are colored dark blue for solar minimum, yellow for rising phase, orange for solar maximum, and light blue for declining phase. (b) Time series of solar activity index (SAI), in the same format. (c) Time-longitude plot of the equatorial solar wind speed at 21.5 $R_{\odot}$ taken from the MAS solutions; vertical black lines mark periods where Carrington rotations were missing from this data set. (d) CR-averages $\left(\langle V \rangle_{CR}\right)$ of equatorial solar wind speed at 21.5 $R_{\odot}$, (e) CR-standard deviations $\left(\sigma_{CR}\right)$ of equatorial solar wind speed at 21.5 $R_{\odot}$.

traversal path. The bimodal (solar minimum) and less-structured (solar maximum) ambient solar wind are evident. The accompanying plot of solar wind speeds along Earth's path at both 0.1 AU and 1 AU (215 $R_{\odot}$) shows a higher frequency of sharp longitudinal gradients in solar wind speed during solar minimum.

Figure 2 presents an overview of the MAS solutions for the years 1975–2024, that is, CR 1625 to CR 2293, approximately 4.5 solar cycles. The radial solar wind speed at 21.5 $R_{\odot}$ at the solar equator is visualized as a time-longitude plot in panel (c), and summarized in the form of CR-averaged speed, $\langle V \rangle_{CR}$ and CR-variability in speed (standard deviation, σ_{CR}) in the bottom two panels. It is clear that both metrics vary substantially over the 50 years, with generally higher values of both speed and variability during solar minimum than during solar maximum.

Into these ambient solar wind estimates, we introduce CMEs of two types: a statistically average and a typical fast CME. We define them based on their initial speed and angular width using values from Barnard et al. (2022). As such, we characterized the average CME with an initial speed of 495 km s^{-1} and a full angular width of 37.4°. The fast CME has a speed of 1,070 km s^{-1} and a wider angular width of 69.8°.

To determine the solar cycle phase, we used sunspot data from the World Data Center SILSO, Royal Observatory of Belgium, Brussels (Clette & Lefèvre, 2015). Specifically, we use the monthly mean sunspot number (SSN) to compute a solar activity index (SAI), which more easily allows the phase, rather than the magnitude, of the cycle to be used. See also (M. J. Owens, Lang et al., 2020). For each month, SAI was computed as the monthly SNN normalized by the maximum SSN within an 11-year rolling window, centered on that month. This was further smoothed over 18 months to produce contiguous solar minimum, rising, maximum and declining intervals. Using this measure, we divide the solar cycle into four phases: the upper quartile of SAI is used to define solar maximum, the two middle quartiles as the transition phases, and the lower quartile as solar minimum. The transition phases were further divided into rising and declining phases by finding the sign of the slope/derivative. Values for SSN and SAI are shown in the top panels of Figure 2, color-coded by phase. It shows that our considered time period covers 4.5 solar cycles. Using SAI thresholds, rather than SSN thresholds, means that almost equal portions of each solar cycle are included in the different activity levels, regardless of the magnitude of the cycle.

2.2. HUXt

HUXt (heliospheric upwind extrapolation with time-dependence) is a reduced-physics solar wind model (M. Owens et al., 2020; Barnard & Owens, 2022). For solar wind flow, it provides similar results to 3-D MHD models. It is essentially a time-dependent version of the Heliospheric Upwind eXtrapolation (HUX) model (Riley & Lionello, 2011), enabling the incorporation of transient events such as CMEs. HUX (and consequently HUXt) assumes the solar wind is a one-dimensional and hydrodynamic flow and approximates the fluid momentum equation as the inviscid Burgers' equation (Pizzo, 1978; Riley & Lionello, 2011). HUXt solves this simplified description of the solar wind numerically using an upwind scheme. M. Owens et al. (2020) showed that HUXt does this for a low computational cost: it took 0.05 s for 27 days of simulation time on a modest desktop CPU, while an MHD model would take 30–60 min on a GPU for the same. This makes it suitable for our study, which requires about 36,000 individual model runs, or around 252,000 simulation days.

Like most current operational space-weather forecasts, HUXt simulates CMEs by adding a quasi-spheroidal speed perturbations to the ambient solar wind at the inner boundary of the model. For a spheroidal CME, the duration of the CME pulse at the inner boundary is determined by the speed and angular width of the CME. M. J. Owens et al. (2025) found that this method creates unrealistic relations between τ and CME parameters. This is because the pulse duration affects how much the solar wind influences CME speed. The result is that we have longer than observed τ for both slow and fast CMEs; slow CMEs have such long pulse durations that they can't be accelerated by the ambient solar wind, while fast CMEs have such short pulse durations that they are too easily slowed by the solar wind. The proposed solution is to fix the pulse duration regardless of CME speed. This effectively mimics CME expansion. In our study, this issue does not apply since we use the same CME with the same speed and angular width, that is, they have the same pulse duration. Even while comparing the two data sets for average and fast CMEs, the fast CME is also wider, hence it complies with CME expansion. Indeed, the average and fast CMEs had pulse durations of 5.7 and 5.4 hr, respectively. The difference is negligible, hence they effectively have the same pulse duration making any intra-comparisons valid. Furthermore, the durations were neither extremely long nor short, ensuring sensible interaction with the ambient solar wind.

HUXt also has a functionality for backmapping each solar wind parcel from the inner boundary to a new altitude. We use it here to define solar wind speeds at 21.5 $R_{\odot}$ using values at 30.0 $R_{\odot}$. HUXt does this by accelerating/decelerating the parcel in accordance with HUXt model dynamics, that is, the acceleration profile used by HUXt. This gives us the new speed. Then, it uses the profile to find the time taken for the parcel to traverse between the two heights. This, in conjunction with the solar rotation rate, is used to find the parcel's new longitude (see

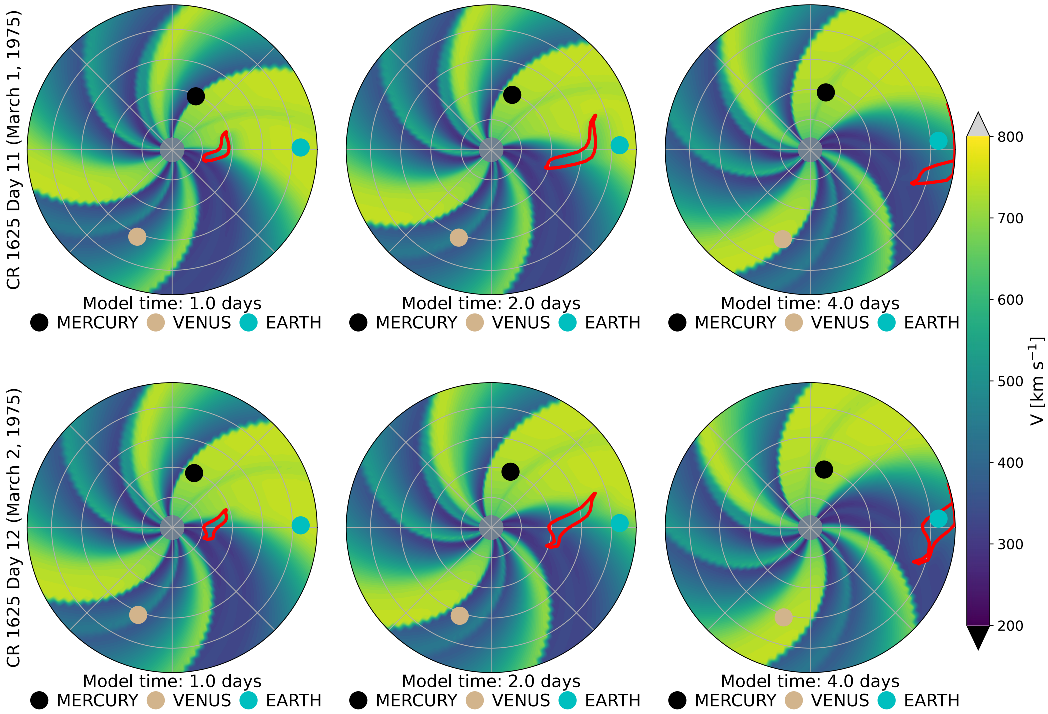

Figure 3. Snapshots of solar wind speed in the solar equatorial plane at three different times (from left to right, shown times 1, 2, and 4 days after CME launch) from two HUXt simulations. Both simulations were run using ambient solar wind conditions for CR 1625 (solar minimum) and contain the average CME, with the CME edge shown as the red contour. Date labels on the left denote initiation time: the top plots were initialized 1 day before the lower plots.

Barnard & Owens, 2022, for detailed methodology). The speed reduction is of the order 5%, and the longitudinal adjustment is a few degrees.

2.3. Experiment Design

To isolate the effect of ambient solar wind on τ and V_{1AU}, we use a consistent model setup across all runs. HUXt simulations are performed on the helioequatorial plane, rather than at the latitude of Earth, which varies slightly throughout the year. The plane was set to have its inner radial boundary at 0.1 AU (21.5 $R_{\odot}$) and an outer boundary at 1 AU (215 $R_{\odot}$), similar to many CME operational forecasts. However, because the MAS solutions of solar wind speed are produced at 30 $R_{\odot}$, we map them to 21.5 $R_{\odot}$ using HUXt's backmapping functionality.

Each MAS solution is based on a Carrington map of the photospheric magnetic field, which is built up over a 27-day period. We perform HUXt runs with a single CME launched directly at Earth. This is repeated once a day through each MAS solution, which is equivalent to launching CMEs through the solar wind structure extracted at longitudes 13.3° apart. Each simulation was run for 7 model days to capture the full CME propagation to Earth. Simulations were run in the sidereal reference frame. For each CME, we record the arrival time and speed of the CME front as it first intercepts the outer boundary at 1 AU. In HUXt, this front is defined using passively-advecting tracer particles, introduced at the CME leading and trailing edges (see Barnard & Owens, 2022).

Figure 3 shows snapshots of solar wind speed in the equatorial plane for two HUXt simulations during CR 1625 (19 February 1975–18 March 1975) around the time of solar minimum. The two runs are both for the average CME, but with a CME initiation time one day apart (equivalent to 13.3° in longitude apart). The different ambient solar wind encountered by the CMEs causes a significant difference in arrival time and speed. When the CME is sped up by a region of fast ambient solar wind, it arrives at Earth in 2.5 days with a speed of 654 km s^{-1}. Initiating it a day later causes the CME to miss the fast region, resulting in a longer τ of 3.1 days and slower V_{1AU} of 504 km s^{-1}.

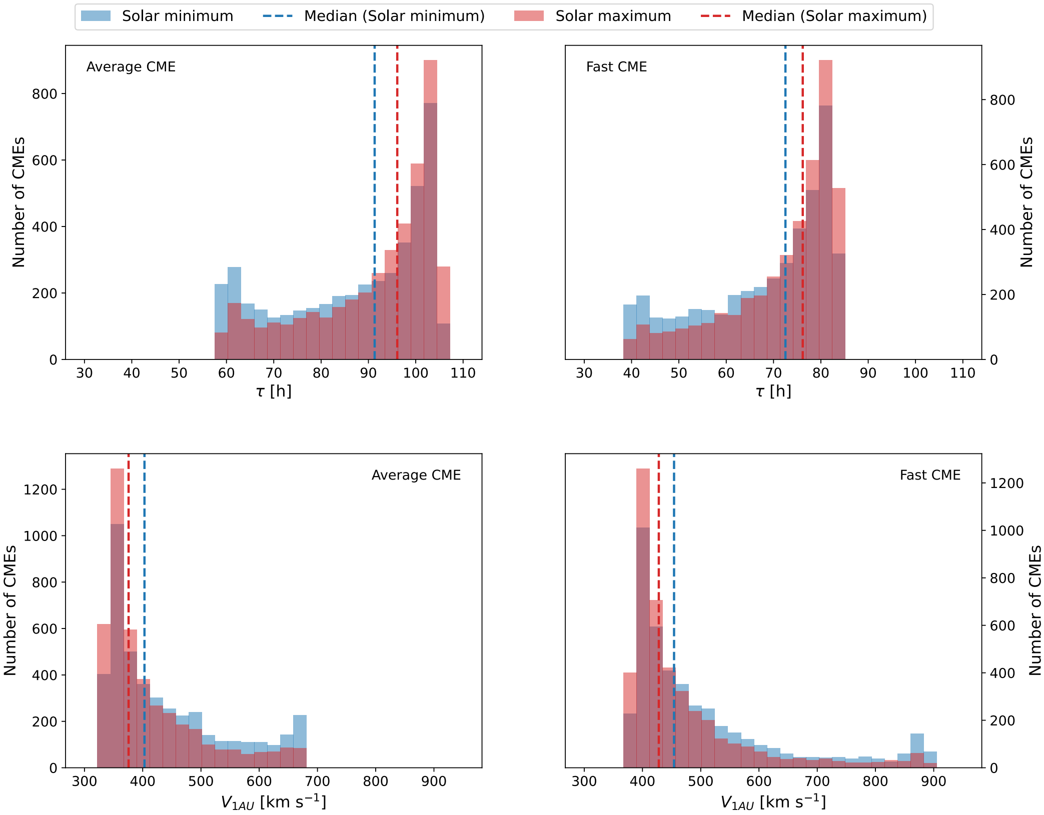

Figure 4. Transit time, τ (top), and arrival speed V_{1AU} (bottom), distributions for individual average (left) and fast (right) CMEs. Solar minimum distribution is colored in blue, while solar maximum distribution is in red. Dotted lines represent medians. All histograms have 30 bins.

3. Results

Figure 4 presents the full distributions of τ and V_{1AU} for both average and fast CME during solar minimum and maximum. Since these distributions are clearly not normal, rank-based statistics are used when required. Variation in the ambient solar wind can change τ for an average CME by up to 47 hr, and a fast CME by 44 hr (exact figures are given in Table 1). The arrival speed of an average CME can vary by up to 340 km s^{-1}, while a fast CME can differ by almost 510 km s^{-1}. While the ranges of τ and V_{1AU} remain similar across the full solar minimum and maximum periods, they exhibit clear solar-cycle differences on shorter time scales, as will be demonstrated.

The τ distributions are particularly bimodal, with peaks at both higher and lower τ. From the median τ values, we see that the average-speed CME typically takes about 5 hr longer to arrive at 1 AU during solar maximum compared to solar minimum. V_{1AU} distributions are less bimodal and more closely resemble a gamma distribution, with a strong peak at lower speeds. The average-speed CME typically arrives about 25 km s^{-1} slower during solar maximum than during solar minimum.

To further investigate the solar cycle variation in CME arrival properties, we next consider how τ and V_{1AU} vary over shorter time scales, by considering values within a given CR. We represent the median values over a CR as $\tilde{\tau}_{CR}$ and $\tilde{V}_{CR}$, and take this as a measure of the most likely value in a given CR. We represent the interquartile range (IQR) over a CR as $IQR_{CR}(\tau)$ and $IQR_{CR}(V)$ and use this as a measure of the variability over a given CR.

The solid lines in Figure 5 show the median values per CR, and the shaded areas span the IQR over a given CR. $\tilde{\tau}_{CR}$ shows modulation with the solar cycle, with generally higher $\tilde{\tau}_{CR}$ values during solar maximum and smaller values during solar minimum. Additionally, we note that the variability bands—which represent $IQR_{CR}(\tau)$—appear broader during solar minimum phases for both average and fast CMEs, except for the narrow band between 1995 and 2000.

Table 1
Median, Range, and Variability of Transit Time, τ and Arrival Speed, V_{1AU} for Average and Fast CMEs Across Solar Cycle Phases

	τ [h]			V_{1AU} [km s^{-1}]		
	Median	Range	$\widetilde{IQR}_{CR}$	Median	Range	$\widetilde{IQR}_{CR}$
Average CME						
Solar minimum	91.3	46.4	22.4	403	336	116
Rising phase	95.8	46.4	16.3	376	336	82
Solar maximum	96.1	46.5	16.4	376	336	76
Declining phase	93.6	46.5	23.8	390	336	126
Fast CME						
Solar minimum	72.5	44.0	18.2	454	504	116
Rising phase	76.6	44.1	13.5	423	505	77
Solar maximum	76.2	44.3	12.5	428	507	70
Declining phase	74.1	44.3	19.2	442	507	121

Note. $\widetilde{IQR}_{CR}$ is the median of $IQR_{CR}(\tau)/IQR_{CR}(V)$ which represents the short-term variability within a carrington rotation.

Figure 5 also shows similar results for V_{1AU}. We see higher $\tilde{V}_{CR}$ during solar minimum, which aligns with its lower $\tilde{\tau}_{CR}$, i.e., higher CME speeds at 1 AU correspond to shorter transit times. Again, the variability bands—representing $IQR_{CR}(V)$—are broader during solar minimum for both CMEs. It is interesting to note that for both CMEs, all $\tilde{V}_{CR}$ values are lower than their respective initial speeds, indicating that strong deceleration during propagation is typical.

Figure 6 shows the distributions of CR-mean properties of τ (i.e., $\tilde{\tau}_{CR}$ and $IQR_{CR}(\tau)$) for solar maximum and minimum. All four distributions for $\tilde{\tau}_{CR}$ are skewed toward longer durations. The median $\tilde{\tau}_{CR}$ values for solar maximum are roughly 5 hr larger than for solar minimum (exact figures are given in Table 1). In comparison, the $(IQR_{CR}(\tau))$ distributions are nearer to normal with less skew. The solar minimum distributions are left-skewed, suggesting that more CR-periods have high variability during solar minimum. Median values of $IQR_{CR}(\tau)$ were typically 6 hr larger at solar minimum than solar maximum for both CMEs.

A similar visualization in Figure 7 shows the same for the CR-mean properties of V_{1AU} (i.e., $\tilde{V}_{CR}$ and $IQR_{CR}(V)$). $\tilde{V}_{CR}$ values are right-skewed, and are typically about 25 km s^{-1} higher during solar minimum. The distributions for $IQR_{CR}(V)$ are also right-skewed, meaning variability is more often low than high. This shape is quite different from that of $IQR_{CR}(\tau)$ in Figure 6. Nevertheless, the main result is the same, with variability being about 40 km s^{-1} higher during solar minimum than during solar maximum.

The histograms presented in Figure 6 are shown as cumulative distribution functions (CDFs) in Figure 8. The $IQR_{CR}(\tau)$ CDFs for solar minimum consistently lie to the right of those for solar maximum, confirming higher variability. In addition to this visual comparison, we apply the two-sample Kolmogorov–Smirnov (KS) test (Massey Jr, 1951) to check whether these differences are statistically significant. The KS test is a nonparametric method that compares the maximum difference (D statistic) between the two CDFs. It does not assume normality, making it well-suited for the skewed distributions considered here. The KS test quantifies the probability that the two CDFs are subsets of the same underlying distribution. We find that the difference in $IQR_{CR}(\tau)$ between solar maximum and minimum has less than a 0.001 probability of resulting from sampling the same distribution. Figure 8 also confirms that $\tilde{\tau}_{CR}$ values are significantly larger during solar maximum.

We also show the CDFs for $\tilde{V}_{CR}$ and $IQR_{CR}(V)$ in Figure 9. The KS test again yielded significant results at the 0.001 level for both CME types, confirming higher variability. It also reaffirms that $\tilde{V}_{CR}$ values are significantly larger during solar minimum.

Exact numeric results characterizing τ and V_{1AU} during the two solar phases are presented in Table 1.

In Figure 10, we extend our comparison of variabilities to include the rising and declining phases. For both $IQR_{CR}(\tau)$ and $IQR_{CR}(V)$, the rising phase shows short-term variability comparable to solar maximum. In fact, it appears to have the least variability for both CME types and both parameters. In contrast, the declining phase resembles solar minimum, showing elevated variability. Its median value consistently ranks the highest out of all four phases.

We also examined solar minimum/maximum phases across individual solar cycles to identify any meaningful cycle-to-cycle differences. Figure 11 shows the cycle-specific distributions of $IQR_{CR}(\tau)$ and $IQR_{CR}(V)$, along with the spread of ambient solar wind speed, (σ_{CR}). We only show values for the average CME here to make the comparison simpler. Most of the solar minimum phases have higher variability than their preceding and succeeding solar maximum phases. Although, we note that the size of this difference is not uniform across cycles. The only exception is the solar minimum phase between cycles 22 and 23. It has abnormally low values for both $IQR_{CR}(\tau)$ and $IQR_{CR}(V)$. The anomaly also manifests in (σ_{CR}), which is much lower for this particular solar minimum phase. It relates back to Figure 5 where we noted unusually low variability during the solar minimum between 1995 and 2000. This is discussed further in Section 4.

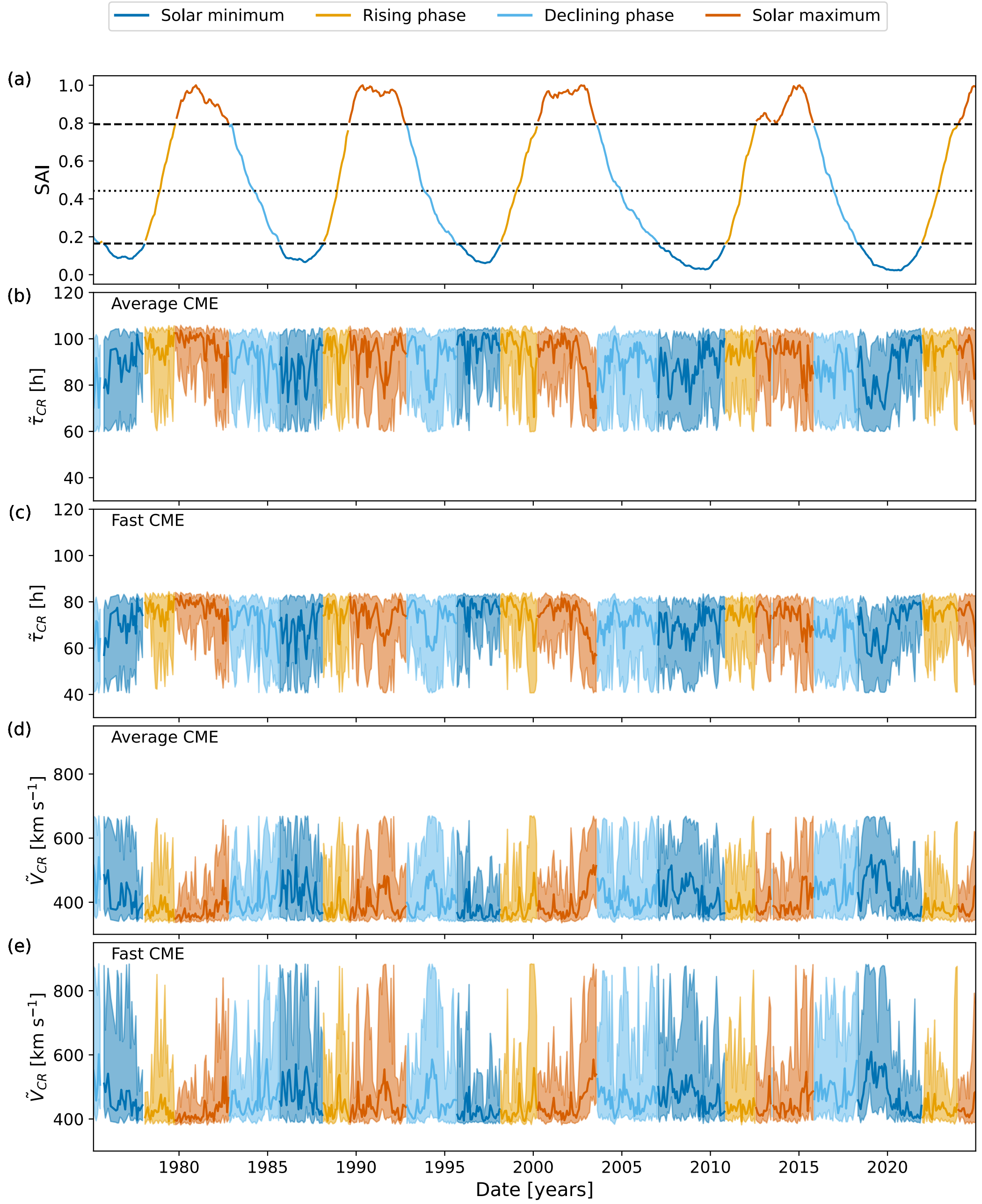

Figure 5. (a) Time series of monthly solar activity index (SAI). Intervals are colored dark blue for solar minimum, yellow for rising phase, orange for solar maximum, and light blue for declining phase. (b) The median τ for a given CR, $\tilde{\tau}_{CR}$, for the average CME. The colored shaded regions span the IQR of τ for a given CR, that is, $IQR_{CR}(\tau)$. (c) The same as panel "b", but for the fast CME. (d) Same as panel "b" but for median V_{1AU} within a given CR, that is, $\tilde{V}_{CR}$ and its IQR, $IQR_{CR}(V)$. (e) Same as the panel "d", for the fast CME.

4. Discussion

This study has investigated the effect of ambient solar wind structure on the transit times and arrival speeds of CMEs over the solar cycle. We numerically simulated the propagation of an average and a fast CME through 50 years of ambient solar wind conditions.

Both CME types had faster propagation and arrival speeds during solar minimum than solar maximum. This is a direct manifestation of fast wind occurring more commonly at lower latitudes during solar minimum than solar

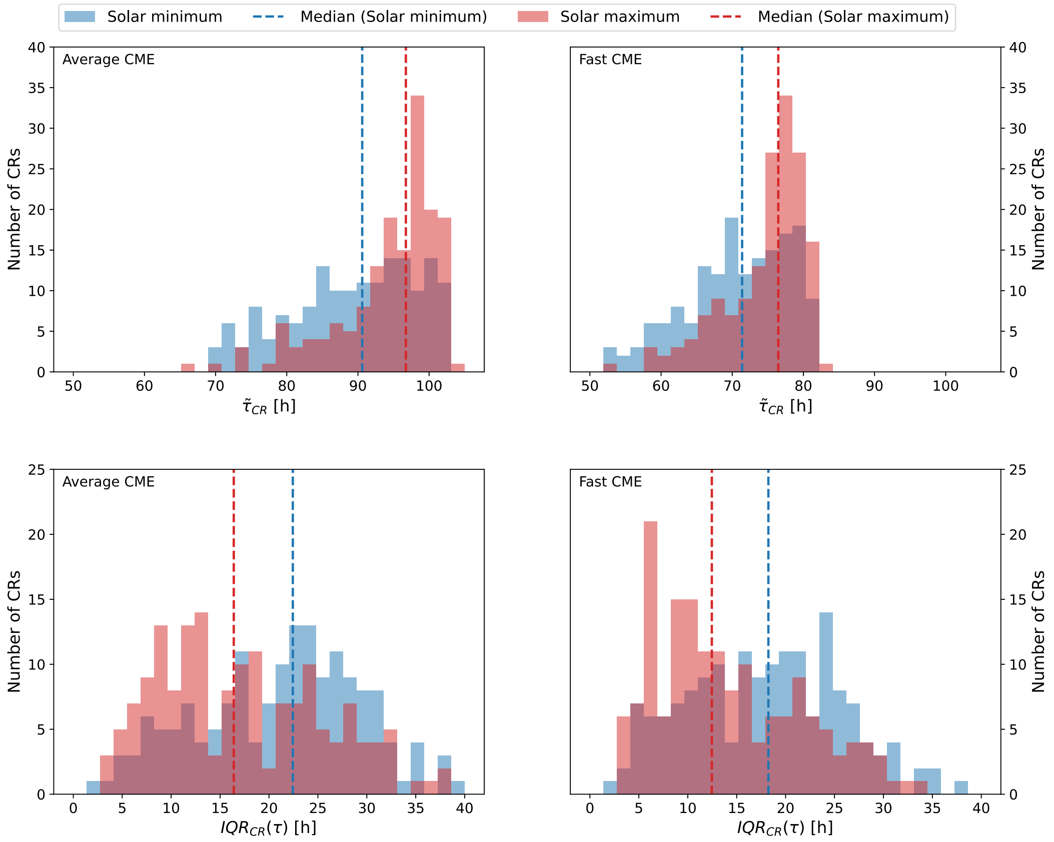

Figure 6. Top: Distributions of median τ within CRs, $\tilde{\tau}_{CR}$, during solar minimum and maximum solar phases for average and fast CMEs. Solar minimum distribution is colored in blue, while solar maximum distribution is in red. Dotted lines represent median values for the distributions. Bottom: The same for distributions of the IQR of τ within CRs, that is, $IQR_{CR}(\tau)$. All histograms have 30 bins.

maximum, that is, CMEs encounter either slow or fast wind during solar minimum, but solar maximum presents mostly slow wind that does not accelerate any CME to the same degree. The τ distribution for individual CMEs revealed a bimodal pattern owing to the dominance of slow and fast solar wind and the comparatively fewer occurrences of "intermediate" wind.

We then considered the spread of τ and V_{1AU} within CRs to evaluate variability patterns over shorter time scales, which may relate more to CME predictability. The variabilities (IQR) of both parameters were systematically larger during solar minimum than during solar maximum. The design of our experiment dictates that this effect purely arises from the change in ambient solar wind structure over a solar cycle. In other words, even identical CMEs can exhibit a range of τ and V_{1AU} within a CR. And the magnitude of this short-term variability changes with the solar cycle, peaking during solar minimum. It implies that in the absence of accurate solar wind forecasts, τ and V_{1AU} are intrinsically less predictable during solar minimum than solar maximum. This is assuming that the CME parameters are perfectly modeled.

Statistically, the variability difference between solar minimum and solar maximum was significant for both V_{1AU} and τ. Despite the statistical significance, in practice, the increase in variability of V_{1AU} during solar minimum—about 40 km s^{-1}—is actually not remarkable. CME initial speeds can only be estimated to within ±200 km s^{-1} (Riley & Ben-Nun, 2021, and references therein), and this uncertainty propagates to arrival speed forecasts. In comparison, a 40 km s^{-1} change in arrival speed error would be trivial.

The motivation for this study comes from real-world forecasting challenges associated with predicting ambient solar wind conditions accurately. e.g., MacNeice et al. (2018, and references therein) assessed several empirical solar wind models used in operations. They found that for a 24-hr lead time, average root-mean-square errors in

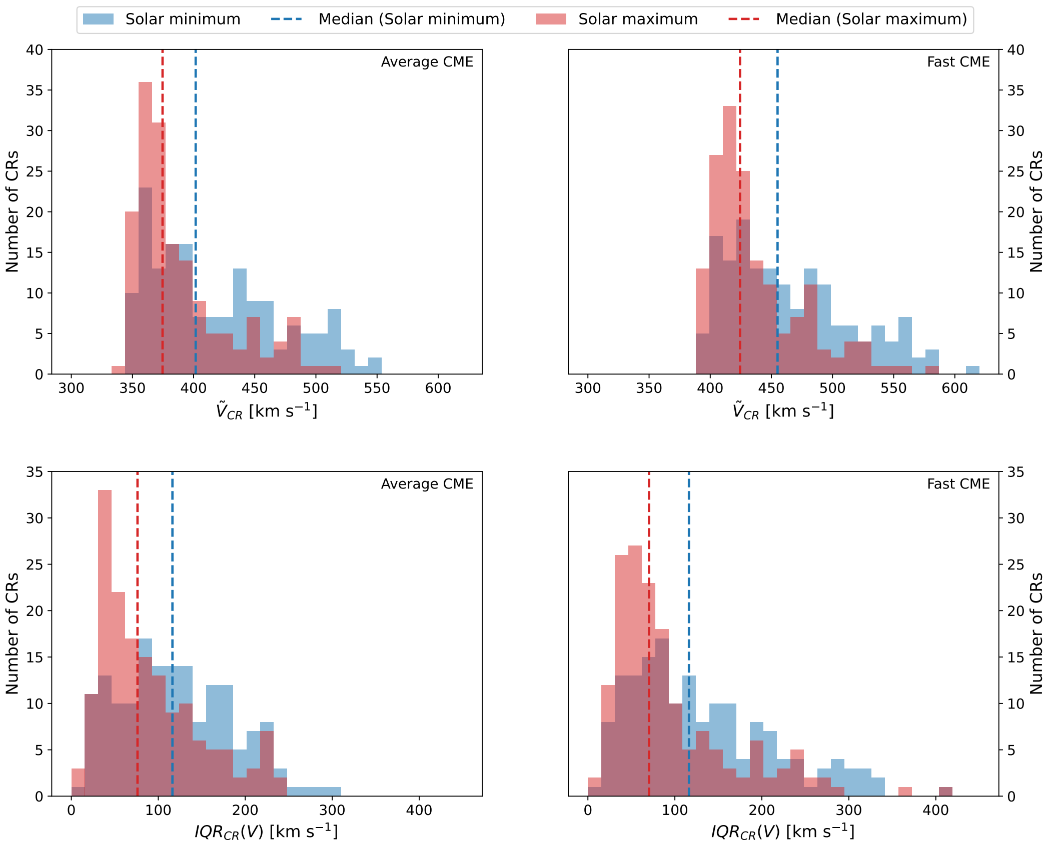

Figure 7. Top: Distributions of median V_{1AU} within CRs, $\tilde{V}_{CR}$, during solar minimum and solar maximum, for average and fast CMEs. Solar minimum distribution is colored in blue, while solar maximum distribution is in red. Dotted lines represent median values for the distributions. Bottom: The same for distributions of the IQR of V_{1AU} for a given CR, that is, $IQR_{CR}(V)$. All histograms have 30 bins.

solar wind speed at L1 ranged from approximately 50 to 110 km s^{-1}, further increasing with lead time. Our results indicate that these errors in background wind will translate to greater τ and V_{1AU} errors during solar minimum.

This point becomes clearer when considering event-specific errors in ambient solar wind forecasting. M. J. Owens et al. (2005) showed that the WSA model made worse predictions at Earth during solar minimum, despite capturing the global structure of solar wind better during this phase. By using a validation approach focusing only on evaluating predictions of high-speed events, they found that small discrepancies in coronal solutions caused large arrival time errors of these events in the ecliptic plane. It ties in with our findings since high-speed events are a feature of the ambient solar wind occurring mostly during solar minimum and the declining phase. More recently, Reiss et al. (2016) showed that operational solar wind models typically predict arrival times of high-speed streams with an uncertainty of about 1 day (if predicted at all). Gressl et al. (2014) found similar results for MHD modeling of the ambient solar wind. Here we have shown that these temporal phase errors could manifest as τ errors of up to 40 hr.

Other sources of uncertainty exist in real events. Generally, solar minimum is associated with easier CME arrival predictions from ambient solar wind interaction, owing to the simpler solar wind structure. CME rates also increase at solar maximum (Gopalswamy et al., 2009), which will lead to an increased probability of CME-CME interactions during propagation to Earth (e.g., Khuntia et al., 2025). We also do not account for magnetic fields and their effect on the heliospheric propagation of CMEs. As CMEs propagate through the magnetized solar wind, interaction with magnetic field structures and plasma flows can distort their morphology. This can cause deformations, front flattening, asymmetric expansion, erosion, deflection, and rotation (see review by Manchester et al., 2017, and references therein).

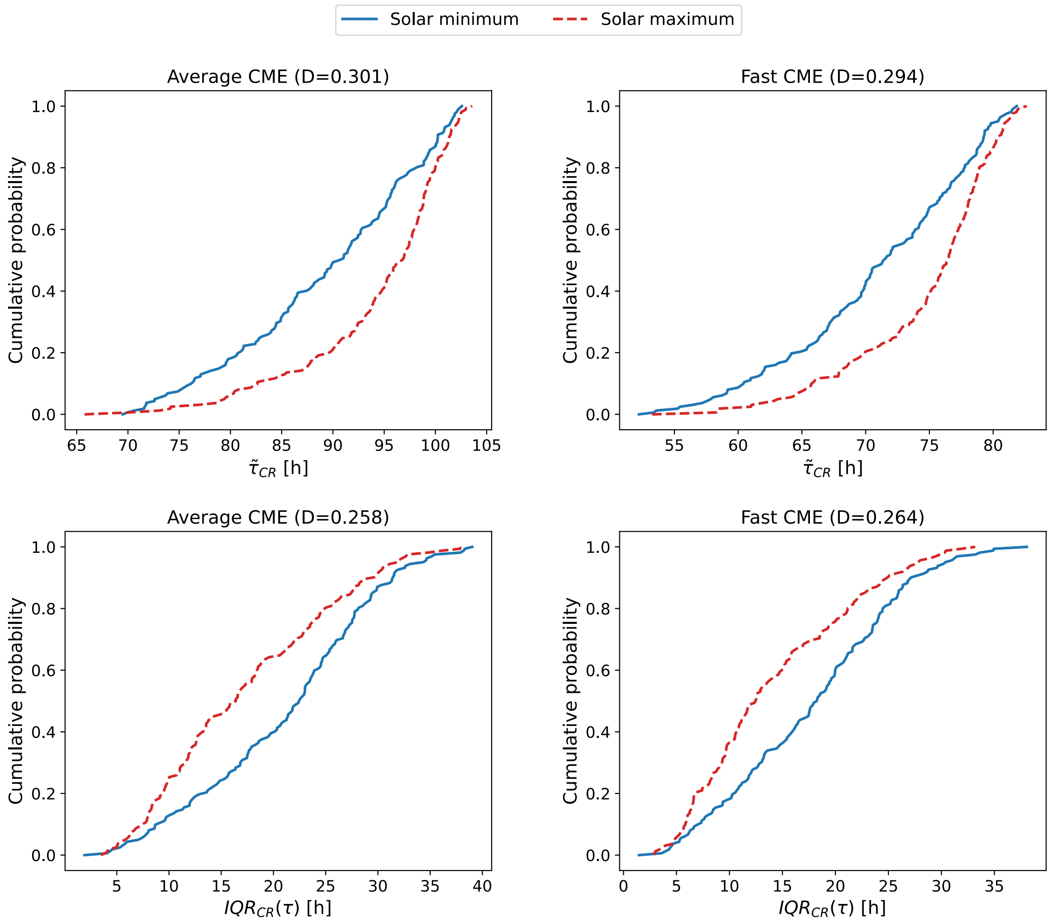

Figure 8. Cumulative distribution functions (CDFs) of median τ within CRs, $\tilde{\tau}_{CR}$, and variability in τ within CRs, $IQR_{CR}(\tau)$, for solar minimum and maximum. D-statistics from the KS test are given.

Accordingly, we compare our results with observed errors in τ forecasts reported in other literature. Kay et al. (2024) found that observed τ errors were higher during solar minimum, and they increase as τ increases. This pattern existed in our results, too, suggesting that a changing ambient solar wind contributes to it. Though direct comparison is difficult, as the CME properties themselves will also have solar-cycle variations.

Magnitude of errors in τ forecasts were found to be on the order of ±10 hr (with a standard deviation of order ±20 hr) by Riley et al. (2018) and Kay et al. (2024), which is of similar order to the variabilities found here. However, this does not mean we can attribute the whole of observed τ errors to ambient solar wind variability. The two are related but not directly comparable. If forecasts used a constant speed for ambient solar wind and had no errors in CME parameters, then errors would be equal to the variabilities presented here. But real life errors can stem from uncertainties in the CME parameters or the ambient solar wind. Riley and Ben-Nun (2021) found an error contribution of ±7 hr from uncertainty in ambient solar wind. That suggests that current forecast schemes capture solar wind variability to some extent but leaves room for improvement. However, it should also be noted that they used an ensemble of ADAPT realizations, which may not encompass the full range of ambient solar wind uncertainties.

We also presented some further analyses that considered other solar cycle phases. The rising phase behaved like solar maximum in terms of variability and the declining phase was comparable to solar minimum. This fits into existing knowledge of the solar wind structure during the transition phases. After solar minimum, the dipolar component of the solar magnetic field weakens in magnitude, and the heliospheric solar wind structure starts resembling solar maximum. On the other hand, the declining phase shows rapid increase in the strength of the solar axial dipole moment, which corresponds to a solar wind configuration similar to solar minimum

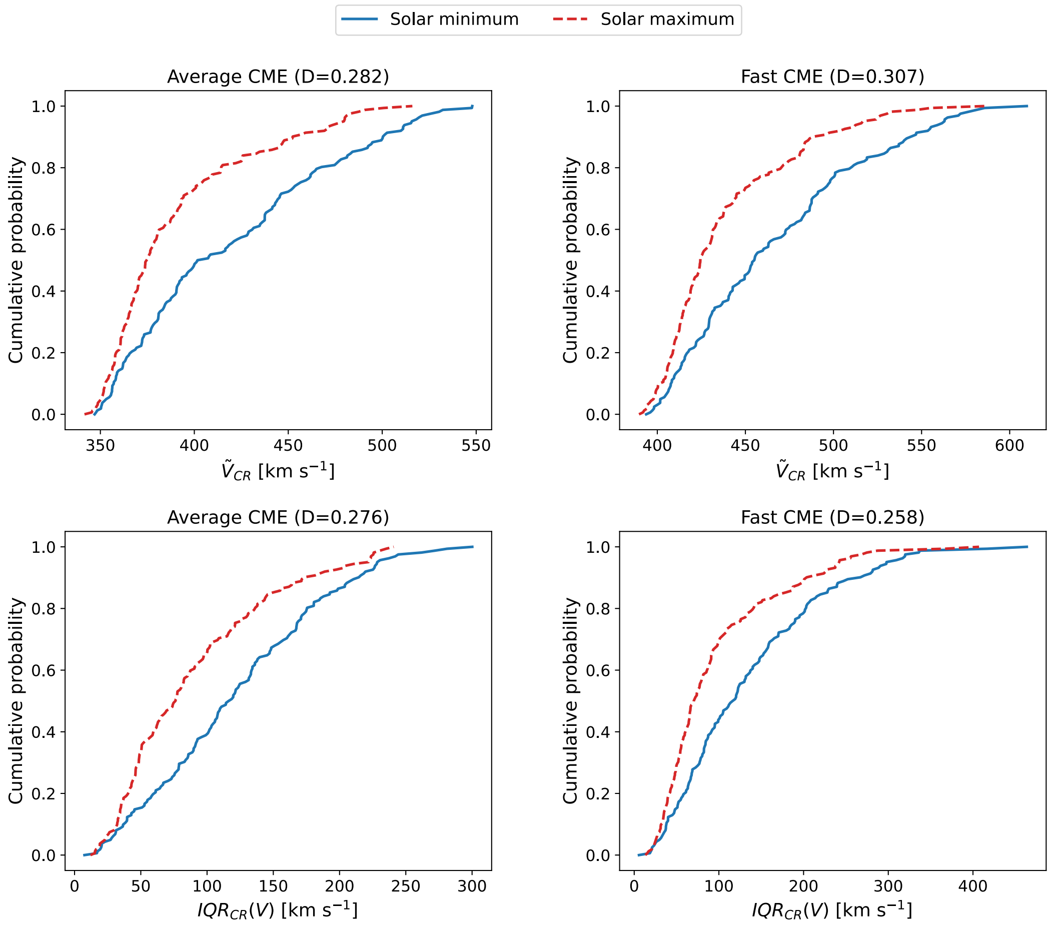

Figure 9. Cumulative distribution functions (CDFs) of median V_{1AU} within CRs, $\tilde{V}_{CR}$, and variability in V_{1AU} within CRs, $IQR_{CR}(V)$, for solar minimum and maximum. D-statistics from the KS test are given.

(Wang, 2024). We can also interpret this with the occurrence rate of high-speed streams in the heliosphere, which peaks during the declining phase, drops sharply after solar minimum, and stays low through solar maximum (e.g., Grandin et al., 2019). This is particularly interesting because the declining phase has been shown to produce CMEs that are more geoeffective than during the rising phase (Lawrance et al., 2020). Combined with higher HSS occurrence and greater unpredictability, the declining phase appears to be a critically important period for space-weather forecasting.

Another investigation involved identifying any cycle-to-cycle changes in this variability pattern. Most cases complied with our general findings. Only one anomalous minimum phase between cycles 22 and 23 showed lower variability than neighboring maximum phases. This seems to stem from the smaller spread in ambient solar wind speeds, which reaffirms the direct correspondence between the two parameters. During this time, the heliospheric current sheet was very flat, as seen from the angular tilt approximated using a potential-field source-surface model (Todd Hoeksema, 1991), and magnetograms from the Wilcox Solar Observatory (not shown here). Accordingly, the MAS solar wind data from this period shows that the streamer belt was tightly confined around the helioequator, with minimal interleaving of high-speed streams. This configuration produced uniformly slow ambient wind, consistent with the observed high median CME transit times and reduced variability in this cycle's minimum. It highlights how each solar cycle is unique; the difference in variability between phases is not fixed. And Earth's position close to the helioequator is particularly sensitive to these second-order changes.

Finally, we recognize that our study had limitations in terms of initial conditions, the use of cone model CMEs, and the range of CME types. Given how ambient solar wind is the sole varying factor in our experiment, further tests employing boundary conditions from different coronal models would ensure the consistency and robustness of our

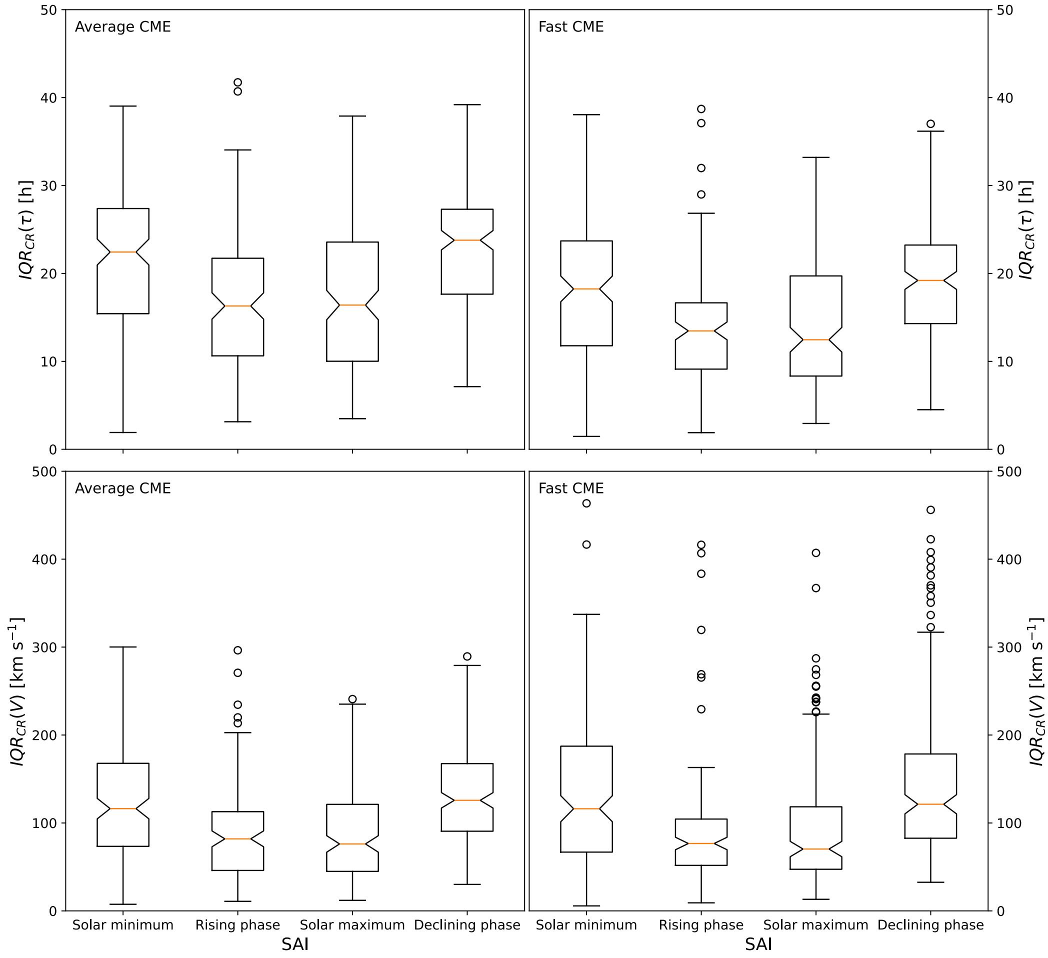

Figure 10. Comparison of variability between different phases of the solar cycle: solar minimum, rising phase, solar maximum, and declining phase. The box and whisker plots show variability in τ within CRs, $IQR_{CR}(\tau)$ (top), and variability in V_{1AU} within CRs, $IQR_{CR}(V)$ (bottom), for average (left), and fast (right) CME.

conclusions. Another possible issue is the cone model representation of a CME used by HUXt. M. J. Owens et al. (2025) points out the implications of this method, highlighting its unphysical tendency to alter CME τ based on CME angular width, which is not observed. Our experiment as a whole is unaffected by this due to the same CME being propagated for all simulations. A possible implication is in our comparison of average and fast CMEs, where angular widths differ. However, the difference in CME duration at the inner boundary was negligible enough. Lastly, using only two types of CMEs reduces our findings to being qualitative. Conducting this experiment with a greater range of CME speeds, widths, and direction of propagation would generate a list of typical transit times/arrival speeds for different CME scenarios, which could be used as a general rule of thumb in operational forecasting. Furthermore, employing ensembles of different boundary parameters in a similar experiment would quantify the sensitivity of arrival properties to each parameter and how it changes over a solar cycle.

5. Conclusion

Investigating the effect of ambient solar wind on CME propagation, we found that variations in the ambient solar wind can shift CME transit time by as much as 47 hr for a statistically average CMEs. Arrival speed varied by 340 km s^{-1}. We also found that this effect varies across the solar cycle. Defining short-term variability in transit time/arrival speed as the interquartile range of their values within a Carrington Rotation, we compared this variability across solar cycle phases. For an isolated and perfectly observed CME, short-term variability in these arrival properties was higher during solar minimum than solar maximum. For an average CME, the mean

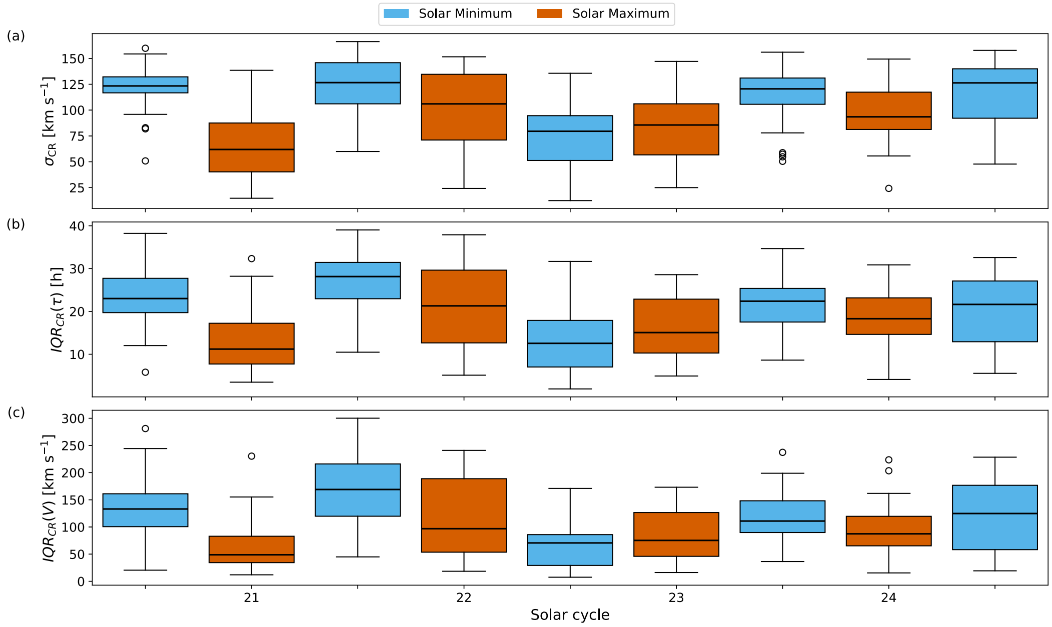

Figure 11. Comparison of variability during solar minimum (blue) and solar maximum (orange) across solar cycles 21, 22, 23, and 24. The box and whisker plots chronologically show (a) variability of ambient solar wind speed at 21.5 $R_\odot$ within CRs, σ_{CR}, (b) variability in τ within CRs, $IQR_{CR}(\tau)$, (c) variability in V_{1AU} within CRs, $IQR_{CR}(V)$. Results are for an average CME.

variability was 22.4 hr during solar minimum and 16.4 hr during solar maximum. This is solely due to the temporal variations in the ambient solar wind.

This has two key implications for CME forecasting. First, when forecasting the arrival properties of a CME, the "true" value exists within a wider range of possible values during solar minimum. Second, the penalty for incorrectly modeling the ambient solar wind—for example, small errors in speed gradients or the position of high-speed streams—is greater during solar minimum. Together, our results present baseline limits of transit time and arrival speed predictability due to ambient solar wind variation, and the increased importance of accurate ambient solar-wind representation during solar minimum.

Conflict of Interest

The authors declare no conflicts of interest relevant to this study.

Availability Statement

The HUXt model was obtained from M. Owens and Barnard (2024).

The MAS solar wind solutions were obtained through the MHDweb modeling website from Predictive Science Inc. https://www.predsci.com/mhdweb/home.php.

All code and data used for this study are available at Gyeltshen et al. (2025).

Acknowledgments

We would like to thank the two anonymous reviewers for their constructive comments. DLG is funded through Science and Technology Facilities Council (STFC) grant ST/Y50916/1. LAB is supported by a UKRI Future Leaders Fellowship MR/Y021207/1. MJO is part-funded by STFC Grant number UKRI1207 and Natural Environment Research Council (NERC) Grant number NE/Y001052/1.

References

Arge, C. N., Henney, C. J., Koller, J., Compeau, C. R., Young, S., MacKenzie, D., et al. (2010). Air force data assimilative photospheric flux transport (ADAPT) model. *AIP Conference Proceedings*, *1216*(1), 343–346. https://doi.org/10.1063/1.3395870

Arge, C. N., Odstrcil, D., Pizzo, V. J., & Mayer, L. R. (2003). Improved method for specifying solar wind speed near the Sun. In M. Velli, R. Bruno, F. Malara, & B. Bucci (Eds.), *Solar wind ten* (Vol. 679, pp. 190–193). AIP. https://doi.org/10.1063/1.1618574

Barnard, L., & Owens, M. (2022). HUXt—An open source, computationally efficient reduced-physics solar wind model, written in Python. *Frontiers in Physics*, *10*, 1005621. https://doi.org/10.3389/fphy.2022.1005621

Barnard, L., Owens, M. J., Scott, C. J., Lockwood, M., de Koning, C. A., Amerstorfer, T., et al. (2022). Quantifying the uncertainty in CME kinematics derived from geometric modeling of heliospheric imager data. *Space Weather*, *20*(1), e2021SW002841. https://doi.org/10.1029/2021SW002841

Bingham, S., Jackson, D., Gonzi, S., Henley, E., Down, E., Sharpe, M., et al. (2018). Operational space weather forecasting at the UK Met Office.

Brueckner, G. E., Howard, R. A., Koomen, M. J., Korendyke, C. M., Michels, D. J., Moses, J. D., et al. (1995). The large angle spectroscopic coronagraph (LASCO). *Solar Physics*, *162*(1), 357–402. https://doi.org/10.1007/BF00733434

Buzulukova, N., & Tsurutani, B. (2022). Space weather: From solar origins to risks and hazards evolving in time. *Frontiers in Astronomy and Space Sciences*, *9*, 1017103. https://doi.org/10.3389/fspas.2022.1017103

Cannon, P. (2013). *Extreme space weather: Impacts on engineered systems and infrastructure*. Royal Academy of Engineering.

Cargill, P. J. (2004). On the aerodynamic drag force acting on interplanetary coronal mass ejections. *Solar Physics*, *221*(1), 135–149. https://doi.org/10.1023/B:SOLA.0000033366.10725.a2

Case, A. W., Spence, H. E., Owens, M. J., Riley, P., & Odstrcil, D. (2008). Ambient solar wind's effect on ICME transit times. *Geophysical Research Letters*, *35*(15), L15105. https://doi.org/10.1029/2008GL034493

Clette, F., & Lefèvre, L. (2015). SILSO sunspot number V2.0 [dataset]. In *World data Center SILSO, royal observatory of Belgium (ROB)*. https://doi.org/10.24414/QNZA-AC80

Eastwood, J. P., Biffis, E., Hapgood, M. A., Green, L., Bisi, M. M., Bentley, R. D., et al. (2017). The economic impact of space weather: Where do we stand? *Risk Analysis*, *37*(2), 206–218. https://doi.org/10.1111/risa.12765

Ebert, R. W., McComas, D. J., Elliott, H. A., Forsyth, R. J., & Gosling, J. T. (2009). Bulk properties of the slow and fast solar wind and interplanetary coronal mass ejections measured by Ulysses: Three polar orbits of observations. *Journal of Geophysical Research*, *114*(A1), A01109. https://doi.org/10.1029/2008JA013631

Gopalswamy, N. (2016). History and development of coronal mass ejections as a key player in solar terrestrial relationship. *Geosci. Lett.*, *3*(1), 8. https://doi.org/10.1186/s40562-016-0039-2

Gopalswamy, N., Lara, A., Lepping, R. P., Kaiser, M. L., Berdichevsky, D., & St. Cyr, O. C. (2000). Interplanetary acceleration of coronal mass ejections. *Geophysical Research Letters*, *27*(2), 145–148. https://doi.org/10.1029/1999GL003639

Gopalswamy, N., Yashiro, S., Stenborg, G., Vourlidas, A., Freeland, S., & Howard, R. (2009). The SOHO/LASCO CME catalog. *Earth, Moon, and Planets*, *104*, 295–313. https://doi.org/10.1007/s11038-008-9282-7

Gosling, J. T. (1993). The solar flare myth. *Journal of Geophysical Research*, *98*(A11), 18937–18949. https://doi.org/10.1029/93JA01896

Grandin, M., Aikio, A. T., & Kozlovsky, A. (2019). Properties and Geoeffectiveness of solar wind high-speed streams and stream interaction regions during solar cycles 23 and 24. *Journal of Geophysical Research: Space Physics*, *124*(6), 3871–3892. https://doi.org/10.1029/2018JA026396

Gressl, C., Veronig, A. M., Temmer, M., Odstrčil, D., Linker, J. A., Mikić, Z., & Riley, P. (2014). Comparative Study of MHD modeling of the background solar wind. *Solar Physics*, *289*(5), 1783–1801. https://doi.org/10.1007/s11207-013-0421-6

Gyeltshen, D. L., Barnard, L., & Owens, M. (2025). Code and data for "why cmes arrive differently: Solar cycle modulation through solar wind structure". *Zenodo*. https://doi.org/10.5281/zenodo.17750335

Howard, R. A., Moses, J. D., Vourlidas, A., Newmark, J. S., Socker, D. G., Plunkett, S. P., et al. (2008). Sun Earth connection coronal and heliospheric investigation (SECCHI). *Space Science Reviews*, *136*(1), 67–115. https://doi.org/10.1007/s11214-008-9341-4

Kay, C., Palmerio, E., Riley, P., Mays, M. L., Nieves-Chinchilla, T., Romano, M., et al. (2024). Updating measures of CME arrival time errors. *Space Weather*, *22*(7), e2024SW003951. https://doi.org/10.1029/2024SW003951

Khuntia, S., Mishra, W., & Agarwal, A. (2025). Evolution of the interacting coronal mass ejections that drove the great geomagnetic storm of 10 May 2024. *Astronomy and Astrophysics*, *698*, A79. https://doi.org/10.1051/0004-6361/202452866

Lawrance, M. B., Moon, Y.-J., & Shanmugaraju, A. (2020). Relationships between interplanetary coronal mass ejection characteristics and Geoeffectiveness in the declining phase of solar cycles 23 and 24. *Solar Physics*, *295*(4), 62. https://doi.org/10.1007/s11207-020-01623-1

Linker, J. A., Mikić, Z., Biesecker, D. A., Forsyth, R. J., Gibson, S. E., Lazarus, A. J., et al. (1999). Magnetohydrodynamic modeling of the solar corona during Whole Sun Month. *Journal of Geophysical Research*, *104*(A5), 9809–9830. https://doi.org/10.1029/1998JA900159

MacNeice, P., Jian, L. K., Antiochos, S. K., Arge, C. N., Bussy-Virat, C. D., DeRosa, M. L., et al. (2018). Assessing the quality of models of the ambient solar wind. *Space Weather*, *16*(11), 1644–1667. https://doi.org/10.1029/2018SW002040

Manchester, W., Kilpua, E. K. J., Liu, Y. D., Lugaz, N., Riley, P., Török, T., & Vršnak, B. (2017). The physical processes of CME/ICME evolution. Space. *Science Review*, *212*(3), 1159–1219. https://doi.org/10.1007/s11214-017-0394-0

Manoharan, P. (2012). Three-dimensional evolution of solar wind during solar cycles 22-24. *The Astrophysical Journal*, *751*(2), 128. https://doi.org/10.1088/0004-637X/751/2/128

Massey, F. J., Jr. (1951). The kolmogorov-smirnov test for goodness of fit. *Journal of the American Statistical Association*, *46*(253), 68–78. https://doi.org/10.1080/01621459.1951.10500769

McComas, D. J., Barraclough, B. L., Funsten, H. O., Gosling, J. T., Santiago-Muñoz, E., Skoug, R. M., et al. (2000). Solar wind observations over Ulysses' first full polar orbit. *Journal of Geophysical Research*, *105*(A5), 10419–10433. https://doi.org/10.1029/1999JA000383

McComas, D. J., Elliott, H. A., Schwadron, N. A., Gosling, J. T., Skoug, R. M., & Goldstein, B. E. (2003). The three-dimensional solar wind around solar maximum. *Geophysical Research Letters*, *30*(10). https://doi.org/10.1029/2003GL017136

Odstrcil, D. (2003). Modeling 3-D solar wind structure. *Advances in Space Research*, *32*(4), 497–506. https://doi.org/10.1016/S0273-1177(03)00332-6

Oughton, E. J., Hapgood, M., Richardson, G. S., Beggan, C. D., Thomson, A. W. P., Gibbs, M., et al. (2019). A risk assessment framework for the socioeconomic impacts of electricity transmission infrastructure failure due to space weather: An application to the United Kingdom. *Risk Analysis*, *39*(5), 1022–1043. https://doi.org/10.1111/risa.13229

Owens, M., & Barnard, L. (2024). *University-of-Reading-Space-Science/HUXt: Huxt V4.2.0*. Zenodo. https://doi.org/10.5281/zenodo.12772120

Owens, M., Lang, M., Barnard, L., Riley, P., Ben-Nun, M., Scott, C. J., et al. (2020). A computationally efficient, time-dependent model of the solar wind for use as a surrogate to three-dimensional numerical Magnetohydrodynamic simulations. *Solar Physics*, *295*(3), 43. https://doi.org/10.1007/s11207-020-01605-3

Owens, M. J. (2020). Solar-Wind structure. In *Oxford research encyclopedia of physics*.

Owens, M. J., Arge, C. N., Spence, H. E., & Pembroke, A. (2005). An event-based approach to validating solar wind speed predictions: High-speed enhancements in the wang-sheeley-arge model. *Journal of Geophysical Research*, *110*(A12), A12105. https://doi.org/10.1029/2005JA011343

Owens, M. J., Barnard, L. A., Verbeke, C., McGinness, B. P. S., Turner, H., Chi, Y., et al. (2025). Implications of using spheroidal "Cone Model" CMEs in solar-wind models. *Space Weather*, *23*(6), e2025SW004397. https://doi.org/10.1029/2025SW004397

Owens, M. J., Lang, M., Riley, P., Lockwood, M., & Lawless, A. S. (2020). Quantifying the latitudinal representivity of in situ solar wind observations. *Journal of Space Weather and Space Climate*, *10*, 8. https://doi.org/10.1051/swsc/2020009

Owens, M. J., Lockwood, M., & Barnard, L. A. (2020). The value of CME arrival time forecasts for space weather mitigation. *Space Weather*, *18*(9), e2020SW002507. https://doi.org/10.1029/2020SW002507

Owens, M. J., Spence, H. E., McGregor, S., Hughes, W. J., Quinn, J. M., Arge, C. N., et al. (2008). Metrics for solar wind prediction models: Comparison of empirical, hybrid, and physics-based schemes with 8 years of L1 observations. *Space Weather*, *6*(8), S08001. https://doi.org/10.1029/2007SW000380

Pizzo, V. (1978). A three-dimensional model of corotating streams in the solar wind, 1. Theoretical foundations. *Journal of Geophysical Research*, *83*(A12), 5563–5572. https://doi.org/10.1029/JA083iA12p05563

Reiss, M. A., Temmer, M., Veronig, A. M., Nikolic, L., Vennerstrom, S., Schöngassner, F., & Hofmeister, S. J. (2016). Verification of high-speed solar wind stream forecasts using operational solar wind models. *Space Weather*, *14*(7), 495–510. https://doi.org/10.1002/2016SW001390

Richardson, I. G., Cane, H. V., & Cliver, E. W. (2002). Sources of geomagnetic activity during nearly three solar cycles (1972–2000). *Journal of Geophysical Research*, *107*(A8), SSH8–1–SSH8–13. https://doi.org/10.1029/2001JA000504

Riley, P., & Ben-Nun, M. (2021). On the sources and sizes of uncertainty in predicting the arrival time of interplanetary coronal mass ejections using global MHD models. *Space Weather*, *19*(6), e2021SW002775. https://doi.org/10.1029/2021SW002775

Riley, P., Linker, J. A., Lionello, R., & Mikic, Z. (2012). Corotating interaction regions during the recent solar minimum: The power and limitations of global MHD modeling. *Journal of Atmospheric and Solar-Terrestrial Physics*, *83*, 1–10. https://doi.org/10.1016/j.jastp.2011.12.013

Riley, P., & Lionello, R. (2011). Mapping solar wind streams from the Sun to 1 AU: A comparison of techniques. *Solar Physics*, *270*(2), 575–592. https://doi.org/10.1007/s11207-011-9766-x

Riley, P., Mays, M. L., Andries, J., Amerstorfer, T., Biesecker, D., Delouille, V., et al. (2018). Forecasting the arrival time of coronal mass ejections: Analysis of the CCMC CME scoreboard. *Space Weather*, *16*(9), 1245–1260. https://doi.org/10.1029/2018SW001962

Shanmugaraju, A., & Vršnak, B. (2014). Transit time of coronal mass ejections under different ambient solar wind conditions. *Solar Physics*, *289*(1), 339–349. https://doi.org/10.1007/s11207-013-0322-8

Temmer, M., Scolini, C., Richardson, I. G., Heinemann, S. G., Paouris, E., Vourlidas, A., et al. (2023). CME propagation through the heliosphere: Status and future of observations and model development. *Advances in Space Research*. https://doi.org/10.1016/j.asr.2023.07.003

Todd Hoeksema, J. (1991). Large-scale solar and heliospheric magnetic fields. *Advances in Space Research*, *11*(1), 15–24. https://doi.org/10.1016/0273-1177(91)90084-W

Vršnak, B., & Žic, T. (2007). Transit times of interplanetary coronal mass ejections and the solar wind speed. *Astronomy and Astrophysics*, *472*(3), 937–943. https://doi.org/10.1051/0004-6361:20077499

Wang, Y.-M. (2024). The radial interplanetary field strength at sunspot minimum as polar field proxy and solar cycle predictor. *The Astrophysical Journal*, *961*(2), L27. https://doi.org/10.3847/2041-8213/ad1c65

Zhao, X., & Dryer, M. (2014). Current status of CME/shock arrival time prediction. *Space Weather*, *12*(7), 448–469. https://doi.org/10.1002/2014SW001060